

# **MWIR Snapshot Imaging Spectrometer: Calibration and Imaging Experiments; Complete Imaging Stokes Polarimeter for The 3 – 5 $\mu\text{m}$ Spectral Band**

March 2000

**C.E. Volin, J.P. Garcia, D.S. Sabatke, E.L. Dereniak, M.R. Descour**

Optical Sciences Center  
University of Arizona  
Tucson, AZ 85721

**T.K. Hamilton, R.W. McMillan**

SMDTC  
Huntsville, Al 35805

## **ABSTRACT**

We report results of experimentation with a new, high-resolution MWIR non-scanning, snapshot imaging spectrometer capable of simultaneously recording spatial and spectral data from a rapidly varying target scene. The instrument is based on computed tomography concepts and operates in a mid-wave infrared band of 3.0 to 5.0  $\mu\text{m}$ . High speed spectral imaging was demonstrated by collecting spectro-spatial snapshots of filtered blackbodies, combustion products and targets of opportunity in the lab. Raw images were recorded using a 512 x 512 InSb focal plane array in snapshot mode.

In addition, a complete Stokes imaging polarimeter for the 3-5  $\mu\text{m}$  band has been constructed and tested. The system features a rotatable form-birefringent retarder, wire grid polarizer and a 512 x 512 InSb array. Design considerations are discussed and results of experiments with man-made and natural targets are presented.

## **MWIR Snapshot Imaging Spectrometer: Calibration and Imaging Experiments.**

### **INTRODUCTION**

Collection of spatial and spectral information has both military and commercial applications, where not only the location of the event is important to the observer but also the spectral content for identification. Up to now, simultaneous imaging and spectrometry were impossible. Spectral images were obtained by scanning in time or space. Recent research developments have produced an imaging spectrometer which simultaneously collects both spectral and 2D spatial information about a scene.<sup>1</sup> To demonstrate our concept, it helps to think of a hyperspectral object cube as shown in Fig. 1.

## Report Documentation Page

<b>Report Date</b> 00032000	<b>Report Type</b> N/A	<b>Dates Covered (from... to)</b> -
<b>Title and Subtitle</b> MWIR Snapshot Imaging Spectrometer: Calibration and Imaging Experiments; Complete Imaging Stokes Polarimeter for The 3 5 $\mu$ m Spectral Band		<b>Contract Number</b>
		<b>Grant Number</b>
		<b>Program Element Number</b>
<b>Author(s)</b> Volin, C.E.; Garcia, J.P.; Sabatke, C. S.; Dereniak, E.L.; Descour, M.R.; Hamilton, T.K.; McMillan, R.W.		<b>Project Number</b>
		<b>Task Number</b>
		<b>Work Unit Number</b>
<b>Performing Organization Name(s) and Address(es)</b> Optical Sciences Center University of Arizona Tucson, AZ 85721		<b>Performing Organization Report Number</b>
<b>Sponsoring/Monitoring Agency Name(s) and Address(es)</b> Director, CECOM RDEC Night Vision and Electronic Sensors Directorate, Security Team 10221 Burbeck Road Ft. Belvoir, VA 22060-5806		<b>Sponsor/Monitor's Acronym(s)</b>
		<b>Sponsor/Monitor's Report Number(s)</b>
<b>Distribution/Availability Statement</b> Approved for public release, distribution unlimited		
<b>Supplementary Notes</b>		
<b>Abstract</b>		
<b>Subject Terms</b>		
<b>Report Classification</b> unclassified	<b>Classification of this page</b> unclassified	
<b>Classification of Abstract</b> unclassified	<b>Limitation of Abstract</b> UNLIMITED	
<b>Number of Pages</b> 15		

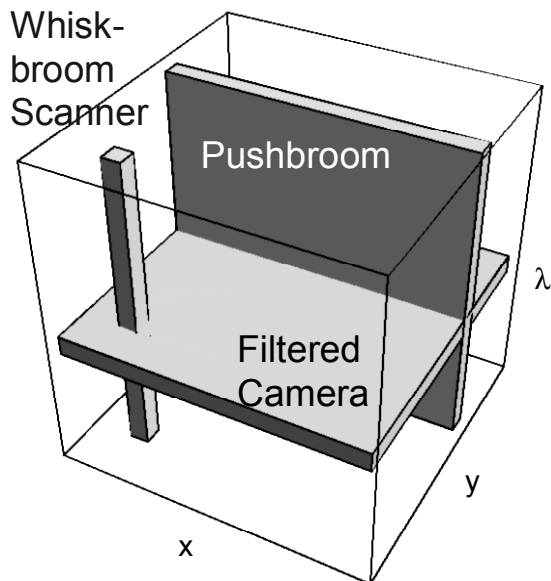


**Fig. 1:** Object cube collected conventionally.

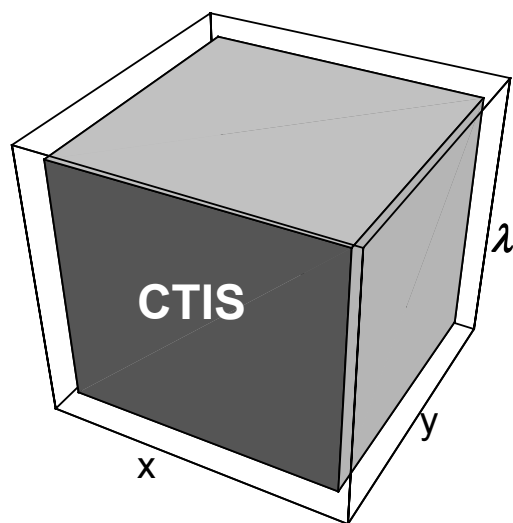


**Fig. 2:** Reconstructed CTIS snapshot object.

The object cube represents the  $x, y, \lambda$  information of a scene. Any slice through the cube parallel to the  $x$ - $y$  plane represents a monochromatic image. Shown in Fig. 1 are different conventional approaches to acquiring the data within the object cube. Note that they all require SCANNING to fill the three dimensional space. The Computed Tomographic Imaging Spectrometer (CTIS) obtains information about the entire object cube each frame time as shown in Fig. 2. This allows reconstruction of spatial and spectral information for the scene at each frame time, which is essential for scenes that change in space/wavelength with time. The CTIS approach to hyperspectral imaging was facilitated by the development of large two-dimensional arrays and fast computing capabilities. In order to acquire the spectra of the scene on a broad-band detector array, an imaging technique, based on computer axial tomography (CAT), was adopted. This combination of technologies allowed the development of a no moving parts, optically simple instrument called CTIS.<sup>2</sup>

## OVERVIEW OF CTIS INSTRUMENT

The driving concept behind the development of the CTIS is the reconstruction of a 3D object from 2D projections. The objective here is to record 2D projections of the  $x, y, \lambda$  object cube. If sufficient projections are recorded, then the original object cube can be reconstructed. These projections are shown schematically in Fig. 3. A two dimensional array records these many “shadows” and reconstruction of the  $(x, y, \lambda)$  object is accomplished via inversion methods.

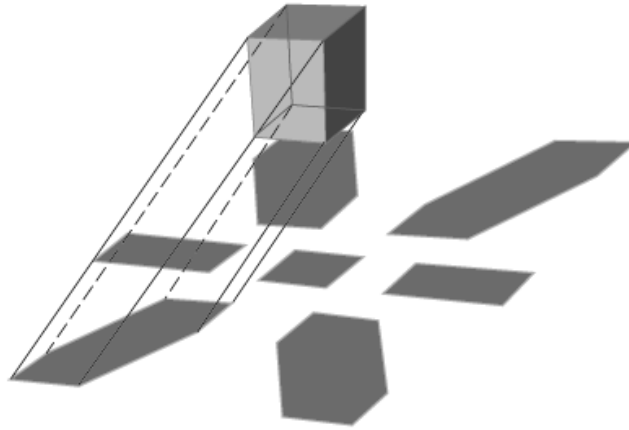


**Fig. 3:** Projections of the object cube onto the focal plane. Spectral information along the vertical axis of the object cube is projected along the radial coordinate of the focal plane and multiplexed with spatial information.

The spectrometer consists of three optical-element groups: an objective lens, a collimator lens, and a re-imaging lens.

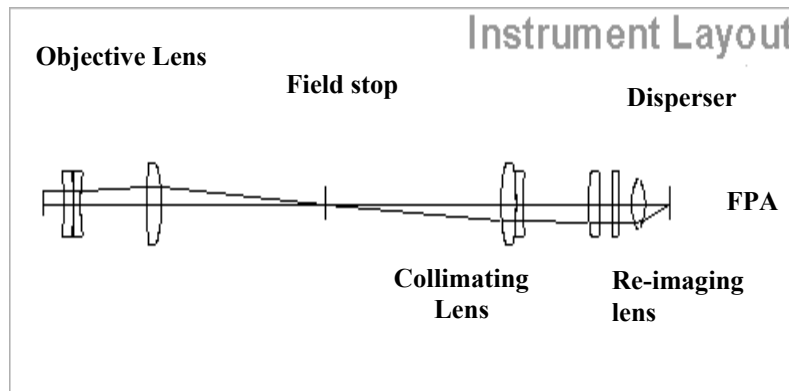


**Fig. 4:** Optical schematic of the CTIS

The use of AR coated lenses for the 3 – 5  $\mu\text{m}$  band in the optical train greatly enhances the performance of the instrument. The Computer Generated Hologram (CGH) disperser<sup>3</sup> is located in collimated space between the collimator lens and the re-imaging lens. The camera in the second generation system shown in Fig 5. uses a 512 x 512 pixel InSb array with 25  $\mu\text{m}$  pitch operating at 60 frames per second and 12 msec. snapshot integration time. The 5mm square field stop maps to a 84 x 84 pixel area on the Focal Plane Array (FPA).

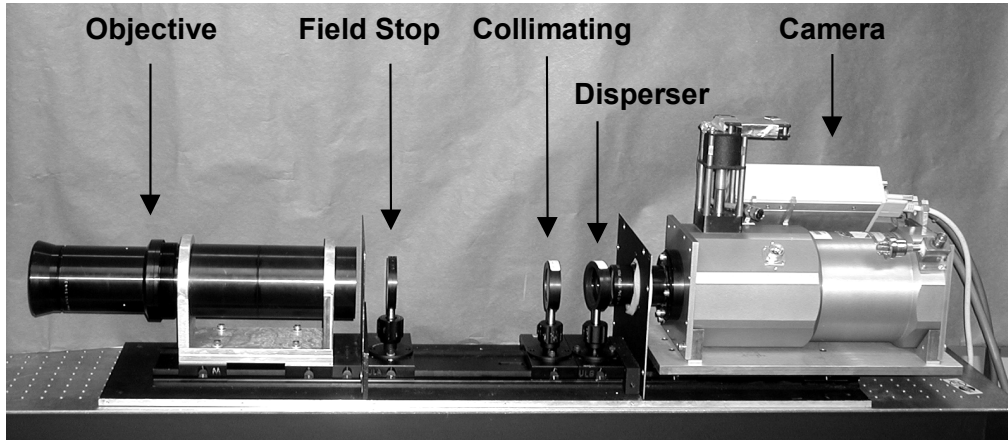


**Fig 5:** Second generation MWIR CTIS. From left to right, a 299 mm focal length objective lens focuses the target onto a 5mm square field stop. The field stop is appropriately minified and dispersed on to the InSb FPA by the combination of a 250 mm collimating lens, GaAs binary diffraction grating and 100 mm re-imaging lens. The re-imaging lens is attached to the liquid nitrogen camera dewar.

While the IR lenses were purchased from vendors, the two-dimensional binary disperser, which is actually a diffractive phase grating, was custom fabricated at the Optical Sciences Center in GaAs. The phase grating shown in Fig. 6, which has a period of  $90\text{ }\mu\text{m}$  in both the x and y directions, was chosen in combination with the field stop size, the collimating lens focal length and the re-imaging lens focal length to place the zero and first diffraction orders within the FPA periphery. The physical depth of the grating was initially chosen to be  $0.7\text{ }\mu\text{m}$  based on a model derived from Goodman's treatment of a sinusoidal phase grating.<sup>4</sup> The depth was subsequently fine tuned by trial and error to  $1.1\text{ }\mu\text{m}$  to give acceptable irradiance uniformity across the FPA.

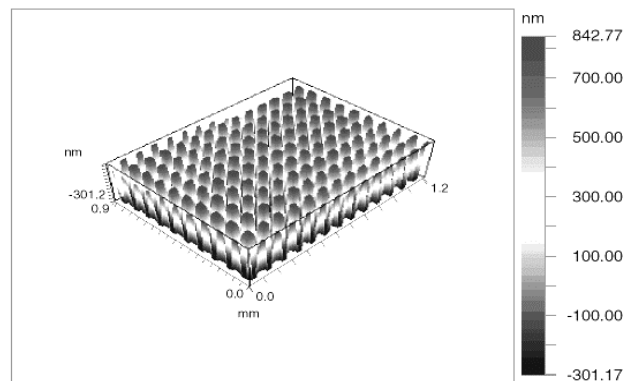


**Fig. 6:** Wyko interferometer surface profile of the 2-D binary phase grating fabricated using Reactive Ion Etching at the Optical Sciences Center by Michael Descour and Daniel Simon.

## CALIBRATION

The MWIR CTIS calibration process was similar to the visible CTIS calibration process. The output port of a commercial blackbody was coupled directly into a computer-controlled monochromator with a 4- $\mu\text{m}$  blazed grating. The monochromator allowed selection of spectral bands as narrow as 0.1  $\mu\text{m}$ . The output of the monochromator was collected by a 36 mm F/1.6 compound lens and launched down a 0.5 meter As-Se-Te fiber. The fiber 250  $\mu\text{m}$  diameter fiber output face was minified into the instrument field stop with a 25 mm Ge lens.

The Ge minifying lens was used to position the calibration spot in the field stop so that nine (25- $\mu\text{m}$ ) pixels were filled on the FPA. The monochromator was then scanned through 21 wavelengths and a calibration image was acquired at each spectral band. Since the instrument is essentially shift invariant over each wavelength, the calibration images were software-shifted to fill the field stop. This technique used to calibrate the MWIR CTIS with  $28 \times 28 \times 21$  (x,y, $\lambda$ ) voxels. There was no allowance for atmospheric absorption over the path difference external to the field stop, but absorption over such a short path should not be significant outside of the CO<sub>2</sub> absorption band from 4.2 to 4.4  $\mu\text{m}$ . Of greater concern is the absorption of the fiber and the spectral variation of the monochromator/blackbody output. These factors will be corrected in future calibrations by use of a reference detector at the focal plane of the Ge minifying lens.

It is not yet established whether the objective lens is exchangeable, as in the visible instrument, under these calibration conditions. Assuming low aberrations from 2.95 to 5.05  $\mu\text{m}$ , (especially distortion) in the objective lenses, it should be possible to exchange objectives without losing calibration accuracy. It is very simple to factor out the ratio of the spectral transmission of the exchanged objectives from the calibration images.

## RESULTS

Preliminary results have been obtained using two laboratory targets. The first was a rear illuminated filter wheel with an open position and a  $3.4 - 4.5 \mu\text{m}$  bandpass filter. A lighter produced hot combustion gases which can be seen in the lower right corner of the raw focal plane image shown below in Fig. 7. Four dispersed orders can be clearly seen, leaving much of the FPA area unused.

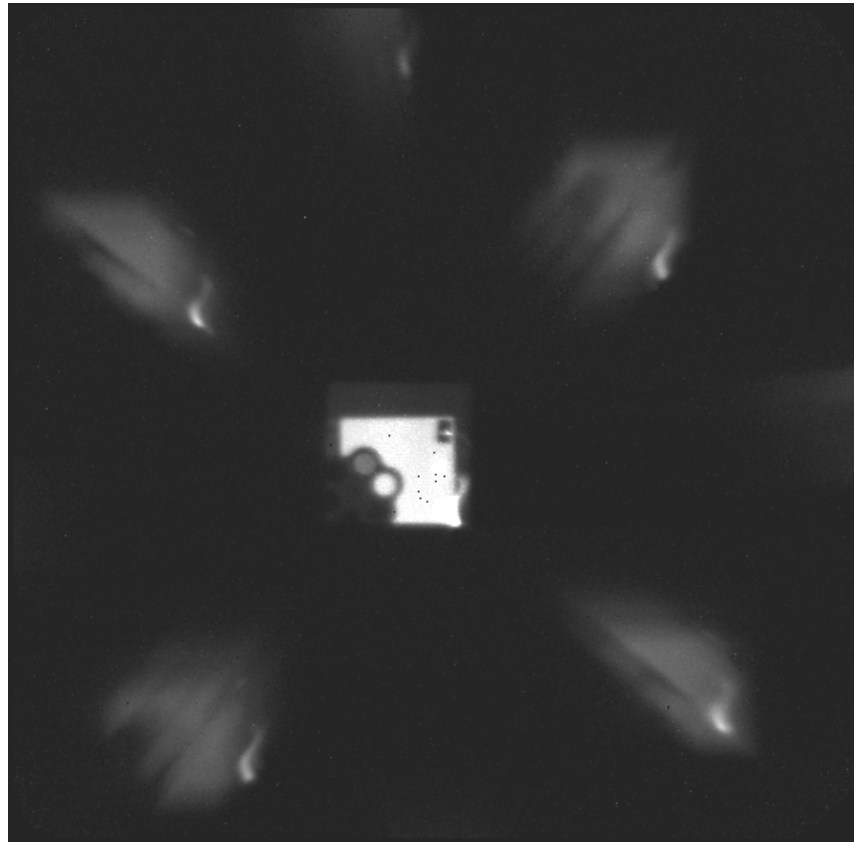


**Fig. 7:** Raw focal plane snapshot image, with background subtraction, of a filter wheel with a  $3.4 - 4.5 \mu\text{m}$  bandpass filter in the upper left position and no filter in the lower right position. A hot plate was used for backlighting. Hot combustion products from a butane lighter can be seen in the lower right corner of the center order. Spectral separation of the combustion gas from the heated plate is evident in all but the center order.

The four primary orders and the center, spectrally compressed, order were used to reconstruct the object via the iterative Multiplicative Algebraic Reconstruction Technique (MART).<sup>5</sup> The grayscale sum of all 21 spectral images is shown in Fig. 8 and the spectra of selected resels are shown in Fig. 9 below.

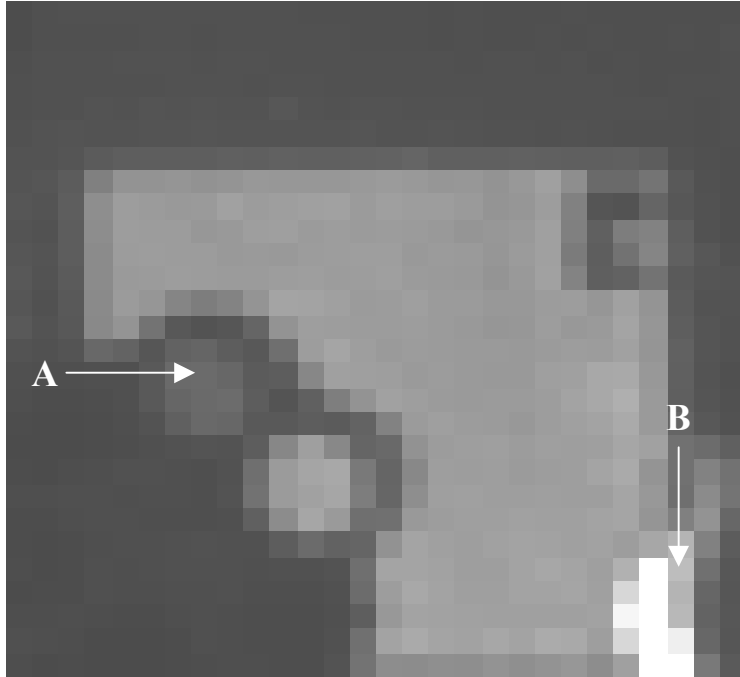


**Fig. 8:** Spectral images of the filter wheel and hot gas for all 21 bands of the instrument compressed into a broadband image to show spatial resolution. The image is 28 x 28 resolution elements (resels). Resels A and B have been marked for further examination.

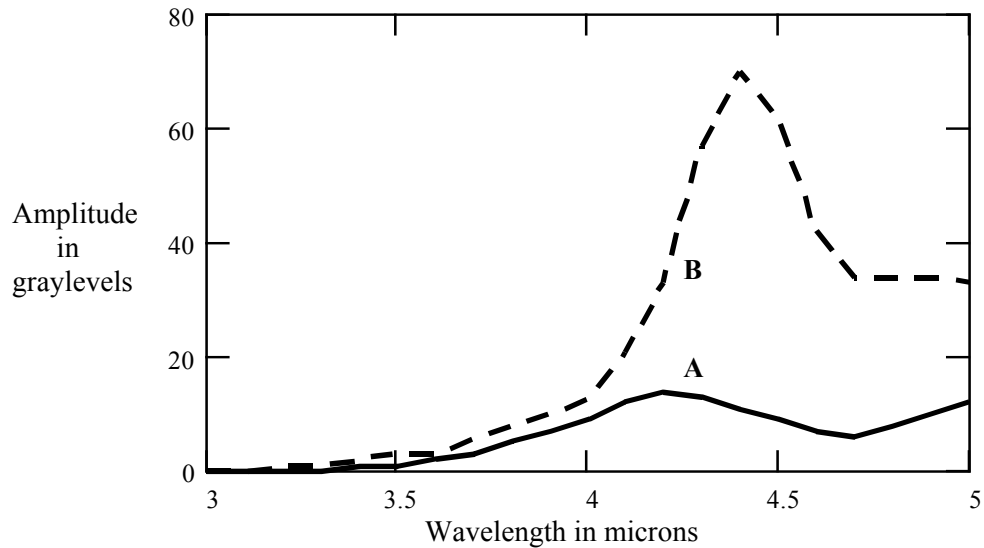


**Fig. 9:** Spectra of resels designated A and B in Fig. 8. Resel A shows the influence of the 3.4 – 4.5  $\mu\text{m}$  bandpass filter and resel B is dominated by hot  $\text{CO}_2$  emission from the butane lighter. The relative brightness of the two resels is reflected in the amplitudes of their spectra in agreement with Fig. 8.



The second laboratory target was a cup of hot coffee spot painted with a  $3.39\text{ }\mu\text{m}$  HeNe laser. The coffee level in the cup is apparent in the center order but the laser spot is partially masked by the hot liquid. In the four primary dispersed orders, the laser spot stands out since the system's dispersion places longer wavelengths farther from the center order.

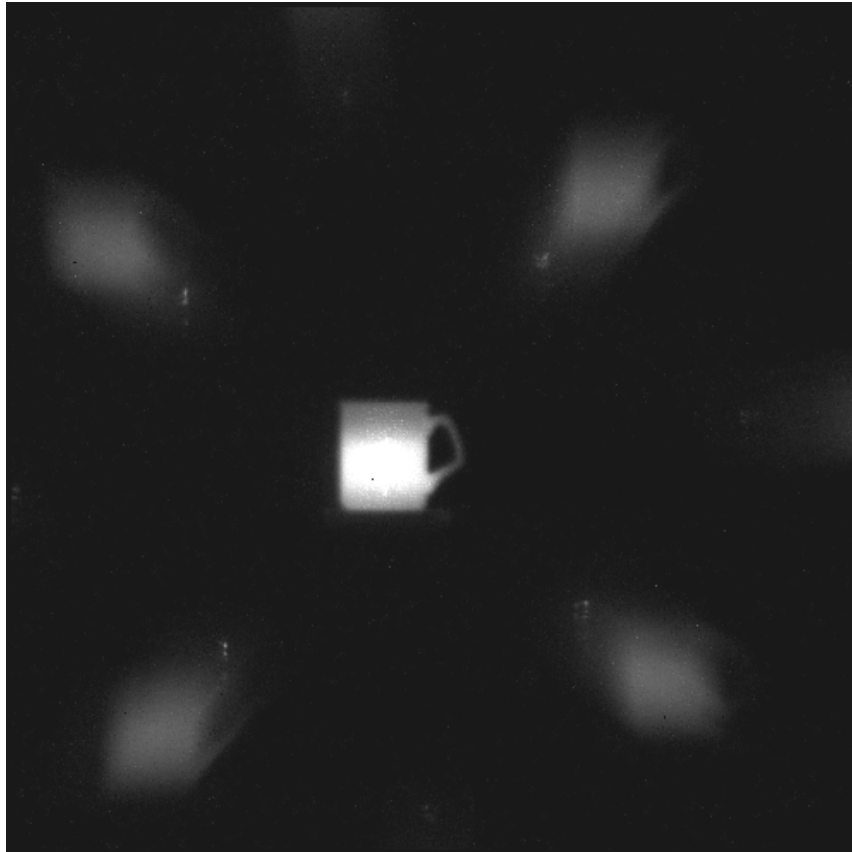


**Fig. 10:** Raw focal plane snapshot image, with background subtraction, of a cup of hot coffee painted by a  $3.39\text{ }\mu\text{m}$  laser in the center warm area. Although the laser spot is not easy to discern in the center broadband order, spectral separation of the spot is obvious in the four primary dispersed orders on the diagonals.

Because of its ability to resolve sharp spectral features such as emission lines, the Expectation Maximization (EM) technique<sup>6</sup> was used to reconstruct this test target. Results are shown in Fig. 11 and Fig. 12 below.

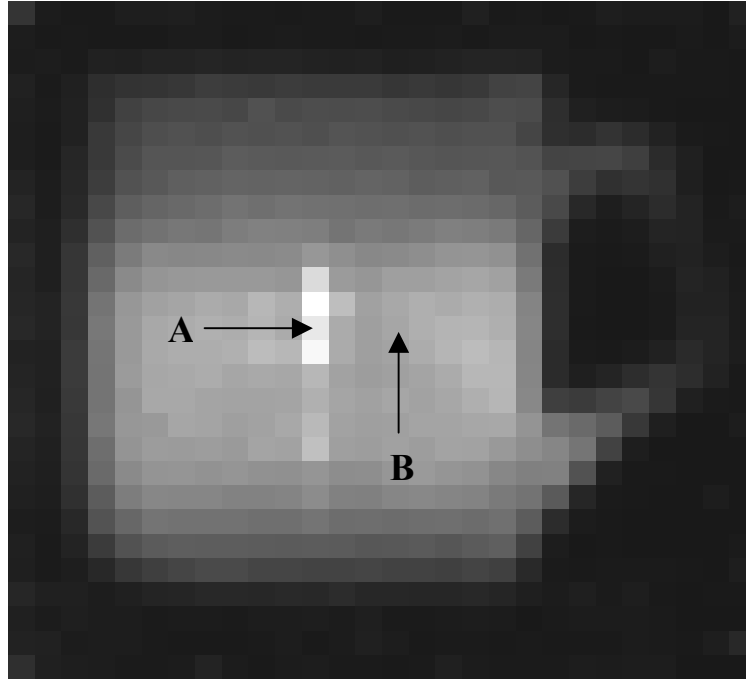


**Fig. 11:** Reconstructed spectral images of the coffee cup and 3.39  $\mu\text{m}$  laser spot for all 21 bands of the instrument compressed into a broadband image to show spatial resolution. The image is 28 x 28 resolution elements (resels). Resels A and B have been marked for further examination. Note the hot liquid level is consistent with Fig. 10.

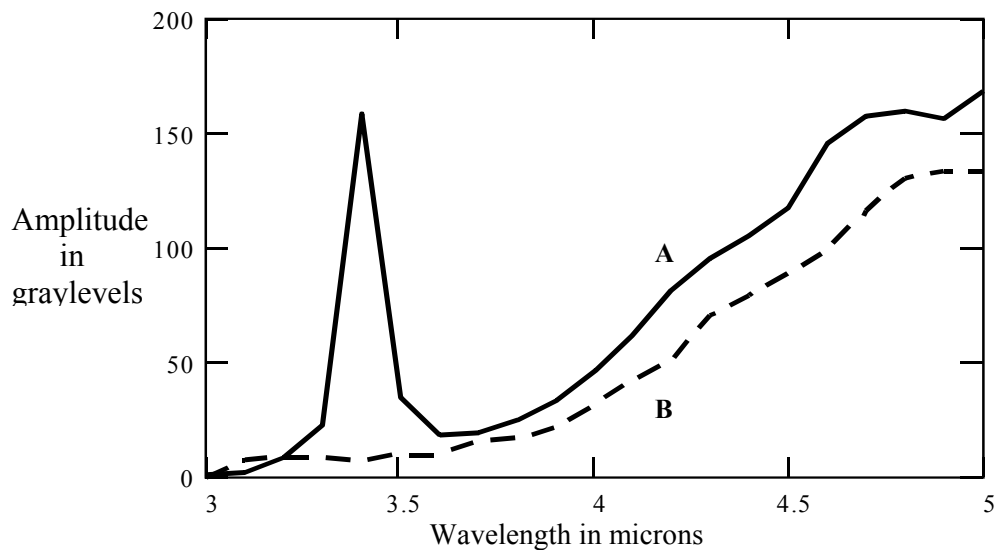


**Fig. 12:** Spectra of resels A and B in Fig. 11 above. Resel A exhibits a strong laser signal in the band centered at 3.4  $\mu\text{m}$  whereas resel B does not. Both resels exhibit spectral consistency beyond 4  $\mu\text{m}$ .

## DISCUSSION

In Figs. 7 – 12, basic functionality of the instrument has been verified. Salient spectral features of both targets have been successfully resolved. The bandpass filter and the hot CO<sub>2</sub> from combustion were reconstructed at the proper spectral wavelength regions in the MWIR for the first target. Likewise, the 3.39  $\mu\text{m}$  laser line peak appeared in the spectral reconstruction band centered at 3.4 $\mu\text{m}$  for the second target. Both spectrally compressed reconstructions in Fig. 8 and Fig. 11 demonstrated sufficient spatial resolution to identify pertinent features of the original scene. For instance, the filter wheel apertures in Fig. 8 and the coffee cup handle in Fig. 11 are clearly identifiable. The instrument is presently limited by the first generation binary diffraction grating which poorly utilizes focal plane array real estate and places a disproportionately large amount of light into the center order. A second generation holographic disperser, which will produce 25 uniform orders, is being fabricated to rectify these problems.

## CONCLUSION

We have demonstrated a high-speed snapshot imaging spectrometer operating in the MWIR. Relative spectral mapping of an object has been demonstrated, although an absolute radiometric calibration of the instrument has not yet been performed. Future work includes performing this calibration to enable absolute temperature mapping and absolute spectral characterization.

## ACKNOWLEDGEMENTS

This work was supported by ARO grant number DAAD 19-99-1-0177 originating from U.S. Army SMDTC, Huntsville, AL. Special thanks go to T.K. Hamilton for providing the large format InSb camera which made this effort possible.

## Complete Imaging Stokes Polarimeter for The 3 – 5 $\mu\text{m}$ Spectral Band

## INTRODUCTION

A MWIR imaging polarimeter has been under development in parallel with the MWIR CTIS. Measurements of the state of polarization of radiation are of interest in remote sensing and reconnaissance. Since radiation emitted or reflected by smooth surfaces tends to take on a polarized component, polarimetry has the potential of aiding detection and identification of manmade objects in natural backgrounds, even when those objects are spectrally camouflaged.

The state of polarization is often described by the Stokes vector  $\mathbf{s}$ . Its first component  $S_0$  represents the total radiance (or other radiometric derivative of power) of a pixel in the target scene. The latter three components ( $s_1$ ,  $s_2$ , and  $s_3$ ) represent respectively preferences for horizontal vs. vertical linear polarization, linear polarization at 45° vs. 135°, and right vs. left-handed circular polarization. A number of other quantities for describing the state of polarization can be defined in term of the Stokes vector.<sup>7</sup>

These include the degree of polarization (*DOP*), the degree of linear polarization (*DOLP*), and the orientation angle  $\eta$  of the major axis of the polarization ellipse.

$$DOP = (s_1 + s_2 + s_3) / s_0 \quad (1)$$

$$DOLP = (s_1 + s_2) / s_0 \quad (2)$$

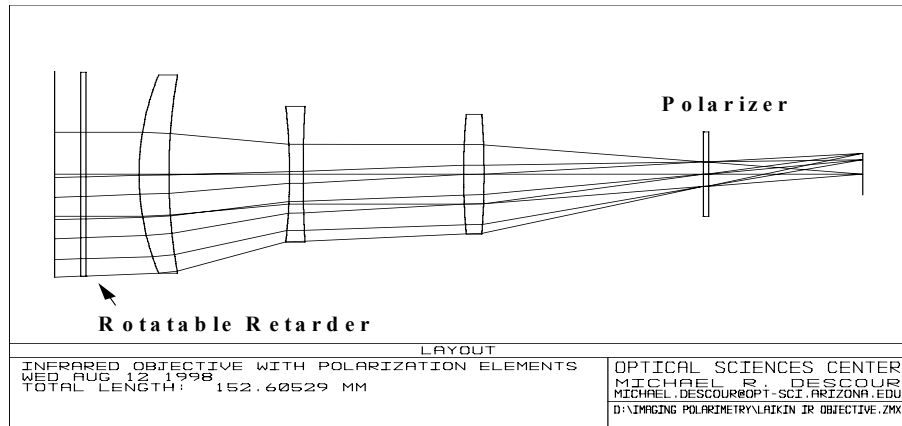
$$\eta = \frac{1}{2} \arctan(s_2 / s_1) \quad (3)$$

The MWIR imaging polarimeter is in particular a complete Stokes polarimeter, meaning it is capable of measuring all four components of the Stokes vector  $s$ . It features a rotatable retarder and fixed linear polarizer in the fore optics (an architecture which will be abbreviated RRFP hereafter). Images are captured with the retarder rotated about the optical axis to each of several predetermined angles, and a Stokes vector estimate for each pixel in the images is reconstructed from this raw data. The choice of values of retardance and retarder orientation angles was made on the basis of the noise sensitivity in the reconstruction step, as will be discussed shortly.

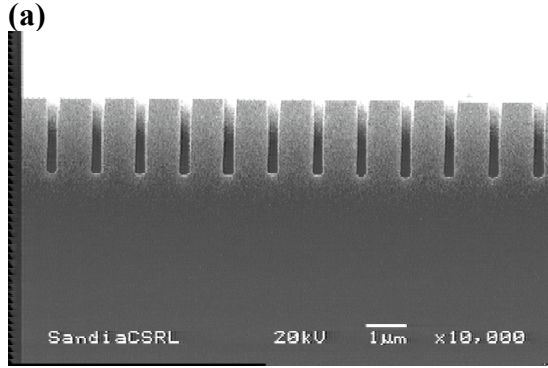
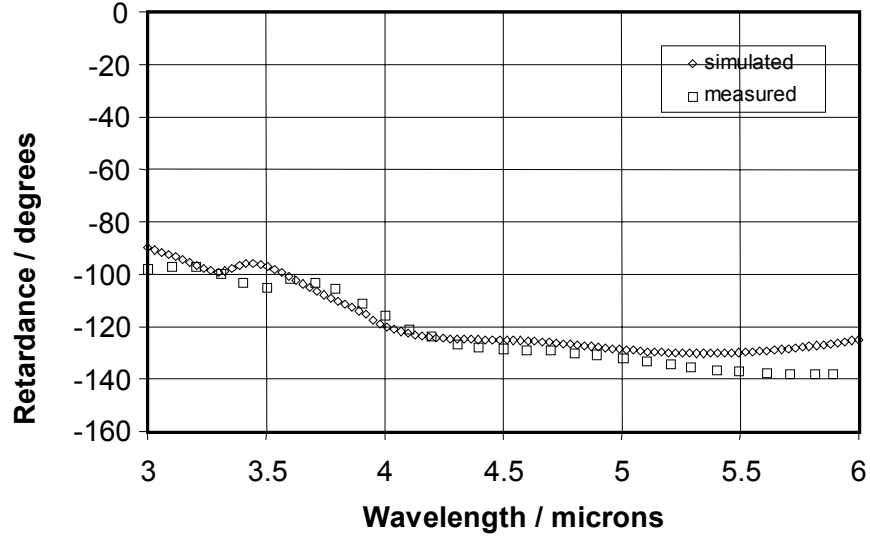
## SYSTEM HARDWARE

Figure 13 contains a representation of the polarization and imaging optics in the polarimeter. A wire grid polarizer (The Optometrics Group, Cat. No. 5-2625) and 4.4 - 5.5  $\mu\text{m}$  bandpass filter are located together in a filter wheel position inside the camera dewar. The retarder is a form-birefringent grating<sup>8</sup> fabricated in GaAs at Sandia National Laboratories (Fig. 14). It has a nominal retardance of  $120^\circ$  in the system's spectral band with was designed to for minimal wavelength dependence in retardance. The retarder exhibits diattenuation with an extinction ratio on the order of 1.5 which is attributable to differences in Fresnel reflection due to the differing effective indices of the TE and TM modes of the grating. The axes of the diattenuation are coincident with the fast and slow axes of the retarder. As a result the diattenuation can be employed to accurately determine the orientation of the wire grid polarizer in the dewar by means of a crossed-polarizer effect.

The 12 bit,  $512 \times 512$  element InSb camera system described in the discussion of MWIR CTIS has been used with this polarimeter. It affords significant improvement over the data obtained during initial system tests with an 8 bit PtSi imager reported in Ref. 9, making new issues of system calibration and characterization accessible to study.



**Fig. 13:** Schematic showing the retarder and polarizer of the RRFP system with an objective lens.



**(b)**  
**Fig. 14:** Part a shows measured and simulated (using rigorous coupled wave analysis) values of retardance of a form-birefringent retarder as a function of wavelength. Part b is a scanning electron micrograph of such an element, showing subwavelength structure. These data refer to a test piece fabricated separately from the retarder used in the polarimeter, and the retardance differs from that quoted in the text. See Ref. 9 for details.

## SYSTEM PERFORMANCE

The retarder's retardance and orientation angles were chosen to minimize the noise sensitivity of the process of reconstructing Stokes vector estimates from the raw data. Sensitivity to noise was characterized by several previously described figures of merit<sup>10</sup> based on the measurement matrix<sup>7</sup> for an RRFP system. The measurement matrix arises in a general linear model of a polarimeter as an instrument which acquires data by measuring the power remaining in a beam after passing through a system of polarization optics described by known Mueller matrices. If a total of  $N$  power measurements  $p_k$ ,  $k \in \{0, 1, \dots, N-1\}$  are made, each through a system of Mueller matrix  $\mathbf{M}_k$ , the measurements are related to the Stokes vector  $\mathbf{s}$  of the incident beam in the absence of noise via

$$\mathbf{p} = \mathbf{W}\mathbf{s}. \quad (4)$$

Here  $\mathbf{p}$  is an  $N$ -element column vector containing the  $p_k$  and  $\mathbf{W}$  is the  $N \times 4$  measurement matrix. The  $k^{\text{th}}$  row of  $\mathbf{W}$  is computed as  $\mathbf{a}^T \mathbf{M}_k$ , where  $\mathbf{a}$  is a 4-element column vector describing the polarization-sensitive responsivity of the detector.

An estimate  $\hat{\mathbf{s}}$  of the incident Stokes vector is generated as

$$\hat{\mathbf{s}} = \mathbf{W}^+ \mathbf{p}. \quad (5)$$

Here a superscripted  $+$  represents the pseudoinverse<sup>11</sup> operation. The pseudoinverse is used for generality, since it can be applied even when  $\mathbf{W}$  is not invertible. In the case of  $N=4$  measurements, however, a complete polarimeter will by definition have an invertible measurement matrix. In order to describe a real system in which noise is present, Eq. 4 should be replaced by

$$\mathbf{p} = \mathbf{W}\mathbf{s} + \mathbf{n} \quad (6)$$

where  $\mathbf{n}$  is an  $N$ -element noise vector whose elements may be considered random variables. Substitution into Eq. 5 yields a term

$$\boldsymbol{\varepsilon} = \mathbf{W}^+ \mathbf{n} \quad (7)$$

which represents the error due to noise in the Stokes vector measurement. A number of figures of merit have been used to quantify the effect of the system matrix  $\mathbf{W}$  in this term. These include the determinant of  $\mathbf{W}$  and the ratio of its largest to smallest singular values. We prefer a figure of merit which we denote EWV that has a simple interpretation in terms of the noise sensitivity of the reconstruction process. EWV, which stands for equally weighted variance, can be expressed in several forms.

$$EWV = \sum_{j=0}^3 \sum_{k=0}^{N-1} (\mathbf{W}^+)^2_{j,k} = \text{Tr}\{(\mathbf{W}^+)^T \mathbf{W}^+\} = \sum_{j=0}^{R-1} 1/\mu_j^2 \quad (8)$$

Here the  $\mu_j$  are the singular values of  $\mathbf{W}$  and  $R$  is its rank. ( $R=4$  for the case of a complete polarimeter.) In the case that the components of  $\mathbf{n}$  are independently random with the same variance  $u$ , EWV is equal to the sum of the variances of each of the components of  $\hat{\mathbf{s}}$  normalized by  $u$ . It is proportional to an average (over the components of the Stokes vector) of the gain in variance incurred in the reconstruction.

Numerical minimization of the EWV for a RRFP system (using  $N=4$  measurements with a polarization insensitive detector with unit responsivity and optics of unit transmittance) yields an optimum value of  $132^\circ$  (approximately  $3/8$  wave) for the retardance.<sup>10</sup> The value of EWV at the minimum is 10.0. Optimum values for the retarder orientation angle for each measurement were also obtained from the optimization. The resulting configuration is also optimal with respect to the measurement matrix determinant and the ratio of its largest to smallest singular values.

The form-birefringent retarder was designed for the optimal retardance of  $132^\circ$ , and the actual value was measured at  $116.8^\circ$ . Retarder orientation angles for use in practice were chosen via a similar optimization using a system matrix which accounts for the diattenuation of the retarder and the actual retardance. The resulting angles are  $\pm 53.7^\circ$ ,  $\pm 15.6^\circ$  (between the retarder's fast axis and the transmissive axis of the polarizer). The EWV of the measurement matrix when these angles are used and diattenuation is included is increased moderately to 14.6.

We have found it necessary to subtract a pedestal image from each raw image of the target scene before reconstructing Stokes vector estimates. Offsets due to fixed pattern noise in the camera system and narcissus effects in the optics can be eliminated in doing so. Since narcissus effects vary with rotations of the retarder, a separate pedestal image is necessary for each retarder orientation angle. Ideally the pedestal images would be obtained by filling the field of view with a cold object in the object plane. This is sometimes possible in a laboratory setting, but may be unrealistic in a remote sensing scenario. An alternative is to capture the pedestals with a cold baffle immediately in front of the system's aperture. Subtraction of pedestals obtained by this method does not correct for atmospheric emission over the

viewing path, however, which may be important depending on the spectral band in use and the viewing distance.

The spectral band of this instrument was chosen on the long wavelength side of the CO<sub>2</sub> absorption feature in the 3-5  $\mu\text{m}$  atmospheric transmission window in order to minimize sensitivity to reflected solar radiation (and thereby isolate emitted radiation). A LOWTRAN<sup>12</sup> calculation suggests that, depending on humidity, atmospheric emission will make a non-negligible contribution to our system's measurements in the 4.4-5.5  $\mu\text{m}$  band over viewing distances on the order of 100 m. The atmospheric emission will effectively be a superposition of a uniform, randomly polarized field onto the scene, i.e. an addition to the  $s_0$  Stokes component. The DOP and DOLP will be reduced as a result. However the polarization angle  $\eta$ , which is independent of  $s_0$ , will be unaffected and may therefore still be a useful parameter for detection and identification of targets. Nonetheless, it may be necessary to reduce the system's spectral bandwidth or move the band to the short wavelength side of the CO<sub>2</sub> absorption feature to reduce the effects of atmospheric emission.

## CONCLUSION

Careful treatment of such concerns as atmospheric emission are necessary before precise Stokes vector measurements are possible. Fig. shows qualitative results of a laboratory test in which the target was a wire grid polarizer mounted in a rotation stage in front of a wide-aperture blackbody. Specular reflections of the environment from the face of the wire grid polarizer were blocked with a cryogenically cooled baffle during image capture. The face of the polarizer, which was oriented to transmit horizontally polarized radiation, is prominent in the  $s_I$  and  $DOLP$  images.

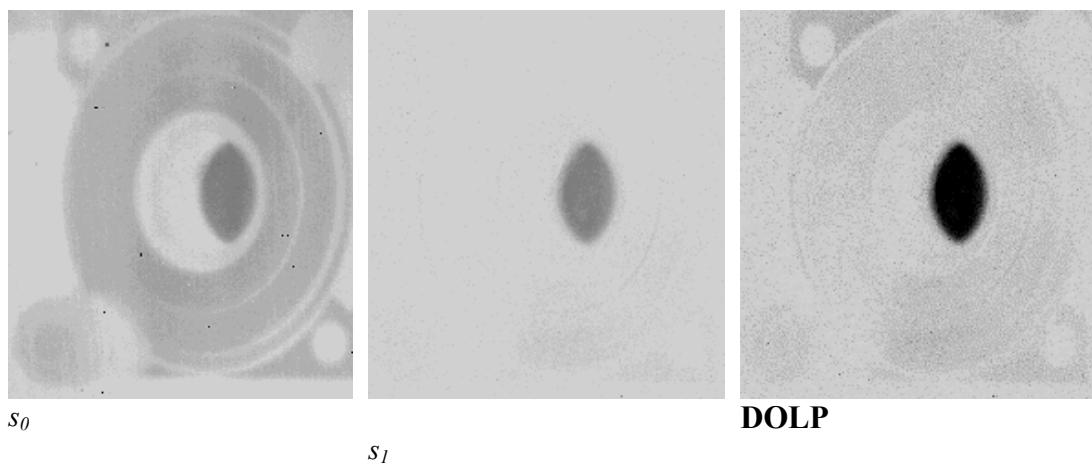


**Fig. 15:**  $s_0$ ,  $s_I$ , and  $DOLP$  images from the experiment described in the text. The  $s_I$  and  $DOLP$  images are displayed in reverse contrast.

## REFERENCES

1. M.R. Descour, C.E. Volin, T.M. Gleeson, M.F. Hopkins, D.W. Wilson, P.D. Maker, "Demonstration of a Computed-Tomography Imaging Spectrometer using a computer-generated hologram disperser", *Applied Optics*, **36**, No. 16, pp. 3694 – 3698 (June 1, 1997).
2. M.R. Descour, C.E. Volin, E.L. Dereniak, K.J. Thome, A.B. Schumacher, D.W. Wilson, P.D. Maker, "Demonstration of a High Speed Non-scanning Imaging Spectrometer", *Optics Letters*, **22**, No. 16, pp. 1271 – 1273 (August 15, 1997).
3. M.R. Descour, C.E. Volin, T.M. Gleeson, M.F. Hopkins, D.W. Wilson, P.D. Maker, "Demonstration of a Computed-Tomography Imaging Spectrometer using a computer-generated hologram disperser", *Applied Optics*, **36**, No. 16, pp. 3694 – 3698 (June 1, 1997).
4. J.W. Goodman, Introduction To Fourier Optics, McGraw-Hill, San Francisco, 1968, pp. 65-70.
5. A. Lent, "A Convergent Algorithm For Maximum Entropy Image Restoration", *Image Analysis and Evaluation, SPSE Conference Proceedings*, Rodney Shaw, ed., pp. 249 – 257 (July 1976).
6. L.A. Shepp and Y. Vardi, "Maximum Likelihood Reconstruction for Emission Tomography", *IEEE Trans. Nucl. Sci.*, **NS-32**, pp. 3864-3872 (1982).
7. R.A. chipman, Chapter 22 in M. Bass, *Handbook of Optics* 2<sup>nd</sup> ed. McGraw-Hill, New York (1995).
8. H. Kikuta, Y. Ohira, and K. Iwata, "Achromatic quarter-wave plates using the dispersion of form birefringence", *Applied Optics*, **36**, No. 17, pp.1566 - 1572 (March 1,1997).
9. G.S. Phipps, *et. al.*, Sandia Report SAND99-2901, 1999.
10. D.S. Sabatke, *et. al.*, "Optimization of Retardance for a Complete Stokes Polarimeter", submitted to Opt. Lett., 2000.
11. G.H. Golub and C.F. Van Loan, *Matrix Computations*. 3<sup>rd</sup> ed. Baltimore: Johns Hopkins, 1996.
12. W.L. Wolfe and G.J. Zissis, *The Infrared Handbook*, revised ed. Washington, DC: Infrared Information Analysis Center, 1993; LOWTRAN 7.2, Ontar Inc.